Nano Research

Open Access

Research Article

Clarifying the effects of oxygenated groups on cobalt-nitrogen-carbon catalysts for H_2O_2 electrosynthesis

Chang Zhang[1,2], Hongshang Hu[3], Wei Liu[1], Huiyao Qi[3], Lilong Zhang[2], Muneerah Alomar[4], Lei Liu[5], Lipiao Bao[1,2], Guanglin Huang[1,2] ✉, Jian Zhang[2,3] ✉, and Xing Lu[1,2] ✉

[1] *School of Materials Science and Engineering, Huazhong University of Science and Technology, Wuhan, Hubei 430074, China*
[2] *School of Chemistry and Chemical Engineering, Hainan University, Haikou 570228, China*
[3] *School of Chemistry and Chemical Engineering, Huazhong University of Science and Technology, Wuhan 430074, China*
[4] *Department of Physics, College of Sciences, Princess Nourah bint Abdulrahman University, P. O. Box 84428, Riyadh 11671, Saudi Arabia*
[5] *Wuxi Zhitai New Energy Technology Co., Ltd., Wuxi 214026, China*

Cite this article: *Nano Research*, **2026**, *19*, 94908416. https://doi.org/10.26599/NR.2026.94908416

ABSTRACT: The incorporation of oxygen functional groups (OFGs) into cobalt-nitrogen-carbon (CoNC) catalysts is widely regarded as a promising strategy for enhancing hydrogen peroxide (H_2O_2) electrosynthesis via the two-electron oxygen reduction reaction ($2e^-$ ORR). However, the roles and effects of OFGs in CoNC catalysts on H_2O_2 electrosynthesis, especially on the actual production, remain unclear. Herein, we conducted a comprehensive investigation into a series of typical CoNC catalysts with or without OFGs for H_2O_2 electrosynthesis. Contrary to the traditional insight, our finding demonstrates that the incorporation of OFGs into CoNC leads to a notable decline in actual H_2O_2 productivity. Remarkably, this phenomenon occurs across diverse oxidizing agents and CoNC catalysts, indicating its generality. Mechanistic investigations reveal that the OFGs regulate the surface chemical states and interfacial hydrophobicities of CoNC, resulting in hindered O_2 diffusion, thus harming H_2O_2 productivity. This study not only clarifies the complex role of OFGs in CoNC catalysts for H_2O_2 electro-synthesis but also promotes their more extensive application in the field of electrocatalyst development.

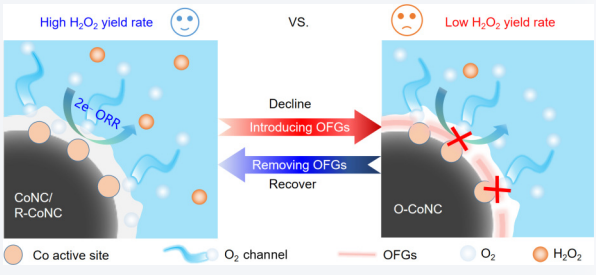

KEYWORDS: cobalt-nitrogen-carbon, catalysts, oxygen functional groups, oxygen reduction reaction, hydrogen peroxide electrosynthesis

1 Introduction

Hydrogen peroxide (H_2O_2) is one of the most important chemicals with wide applications, including industries, medicine, papermaking, and polluted water treatment [1–4]. Currently, the majority of H_2O_2 is produced via an anthraquinone method, which involves complex procedures and huge energy input, and generates lots of organic waste [1–5]. Recently, the emergence of the electrosynthesis process through a two-electron oxygen reduction reaction has attracted extensive attention. It requires only oxygen (from the air), electrolytes, and electricity for the green and sustainable generation of H_2O_2 that is energy-efficient and environmentally friendly [6–12]. However, the key reaction of the two-electron oxygen reduction reaction ($2e^-$ ORR) often suffers from slow kinetics, high overpotential, and the competitive four-electron ($4e^-$) pathway [1–12]. Thus, robust electrocatalysts have been intensively pursued.

Among all the candidates, the oxygen functionalized or coordinated cobalt-nitrogen-carbon (O-CoNC) catalysts reveal great potential for the electrosynthesis of H_2O_2 due to the earth-abundance, considerable ORR activity, and most importantly, much-enhanced $2e^-$ selectivity [4, 13–34]. However, these results are mostly assessed through the rotating ring-disk electrode (RRDE) technique. However, the projection of RRDE-obtained results often only represents the trends, not absolute actual performance values [35]. For H_2O_2 electrosynthesis, the RRDE can measure the ORR activity and $2e^-$ selectivity value, but can not determine the H_2O_2 yield rate (YR) of catalysts. At this point, another measurement of the gas diffusion electrode (GDE) is required [36–39]. Unlike the disk generation and ring *in-situ*

Received: October 15, 2025; **Revised:** December 9, 2025
Accepted: January 7, 2026

✉Address correspondence to Guanglin Huang, guanglinhuang@hust.edu.cn; Jian Zhang, zhangjian7@hainanu.edu.cn; Xing Lu, lux@hust.edu.cn

detection mode of RRDE, the products of GDE naturally diffuse into the solution for further collection or detection [40–43]. This more resembles the actual application and enables researchers to test the productivity of the catalysts. However, compared to RRDE, GDE measurement requires a larger quantity of catalyst, a more intricate process, and a longer duration. Therefore, RRDE is typically employed for the initial screening of numerous promising catalyst materials, while GDE is only used to demonstrate the practical performance of the most crucial sample. As exhibited in Table S1 in the Electronic Supplementary Material (ESM), previous studies reveal that the oxygenated CoNC significantly enhances the H_2O_2 selectivity of pristine catalysts. Note that despite variations in preparation conditions and test protocols, the conclusions drawn are surprisingly consistent. However, they typically only tested the RRDE performance but neglected to compare their GDE performance. Consequently, doubts linger in our minds. How does the H_2O_2 production performance in a real device differ between CoNC catalysts with and without oxygen functional groups (OFGs)? Has the H_2O_2 electrosynthesis performance of CoNC catalysts with OFG modification been genuinely improved when compared to their pristine counterparts? The true functions and effects of OFGs on CoNC catalysts in the synthesis of H_2O_2 remain unclear.

With these questions in mind, we conducted a comprehensive investigation into the performance of a series of typical CoNC catalysts modified with or without OFGs for H_2O_2 electrosynthesis. Our results reveal that the incorporation of OFGs into CoNC markedly reduces the H_2O_2 yield, a trend consistently observed across various oxidizing agents and CoNC systems, underscoring its general applicability. Comprehensive analysis indicates that surface OFGs disrupt the local Co coordination environment, alter the surface chemical state, and enhance hydrophilicity, leading to the destruction of the three-phase interface and hindering the transportation of O_2. Impressively, the removal of OFGs restores the surface interface structure and significantly recovers, or even improves, the H_2O_2 productivity. This work contributes to the recognition and understanding of the effects of OFGs on CoNC catalysts for H_2O_2 electrosynthesis, and most importantly, aims to encourage a more widespread use of practical devices in the evaluation of the catalyst performance.

2 Experimental

2.1 Preparation of zeolitic imidazolate framework-67 (ZIF-67) precursors

Typically, 5.910 g of 2-methylimidazole and 5.244 g of $Co(NO_3)_2{\cdot}6H_2O$ were dissolved in 60 mL of methanol to form solutions A and B, respectively. After that, solution A was rapidly added to solution B with vigorous stirring for 10 s. Subsequently, the resulting mixture was allowed to age at room temperature for 24 h. Finally, the purple precipitate was gathered through centrifugation and subjected to washes with methanol and ethanol. The collected precipitate was then dried in a vacuum oven at 60 °C to obtain the ZIF-67 precursor powder.

2.2 Preparation of CoNC catalysts

The ZIF-67 precursor was transferred to a porcelain boat and then inserted into a tube furnace. After passing for 20 min at a flow rate of 100 mL·min^{-1}, the temperature was increased to 900 °C at a rate of 5 °C·min^{-1} under an Ar atmosphere for 3 h. After fully grinding the carbonized product, it was acid-washed in 0.5 M H_2SO_4 at 60 °C for 6 h to remove cobalt particles. The sample was collected by filtration, washed with ultrapure water until the pH reached 7, and then dried under vacuum overnight. The resulting black powder was named CoNC.

To confirm the universality, other types of CoNC-*X* catalysts (*X* = 1–6) were also prepared using different methods:

200 mg of commercial graphene oxide (GO) was added to 30 mL of ultra-pure water. After ultrasonic dispersion for 30 min, 3 mL of $CoCl_2$ solution (with 3 wt.% Co content) was added under an ultrasonic environment for 1 h and freeze-drying. The precursor was heated to 800 °C at 5 °C·min^{-1} in an NH_3 atmosphere (gas flow rate: 150 mL·min^{-1} Ar and 50 mL·min^{-1} NH_3) for 1 h. After pickling, washing, and drying, the CoNC-1 was obtained.

1.019 g of $Co(NO_3)_2{\cdot}6H_2O$, 2.943 g of dicyandiamide, and 2 mL of anhydrous ethanol were added to the agate mortar and ground continuously until the mixture formed a uniform pink paste. The resulting mixture was transferred to the porcelain boat and then heated to 800 °C at a heating rate of 3 °C·min^{-1} with a flow rate of 100 mL·min^{-1} in the Ar atmosphere for 3.5 h. After pickling, washing, and drying, the CoNC-2 was obtained.

The ZIF-67 precursor was heated to 900 °C at 2 °C·min^{-1} in an Ar/H_2 (10 vol.%) atmosphere with a flow rate of 100 mL·min^{-1} for 1 h. After pickling, washing, and drying, the CoNC-3 was obtained.

The commercial carbon nanotubes (CNTs) were pre-oxidized by concentrated nitric acid at 80 °C for 10 h with magnetic stirring. Then, 100 mg of pre-oxidized CNTs and 10 mg of cetyl trimethyl ammonium bromide (CTAB) were added to the mixed solution of 15 mL of ultra-pure water and 15 mL of ethanol. After ultrasonic dispersion for 30 min, 0.249 g of $Co(NO_3)_2{\cdot}6H_2O$ and 0.497 g of dicyandiamide were added at intervals of 10 min under an ultrasonic environment for 30 min. The precursor was heated to 550 °C at 2 °C·min^{-1} for 1 h and subsequently to 800 °C at 5 °C·min^{-1} for 2 h under an Ar atmosphere with a flow rate of 100 mL·min^{-1}. After pickling, washing, and drying, the CoNC-4 was obtained.

0.249 g of $Co(CH_3COO)_2{\cdot}4H_2O$ and 0.8408 g of dicyandiamide were added to the mixed solution of 10 mL of ultra-pure water and 10 mL of ethanol. After drying by magnetic stirring at 60 °C, the precursor was heated to 800 °C at 5 °C·min^{-1} for 2 h under an Ar atmosphere with a flow rate of 100 mL·min^{-1}. After pickling, washing, and drying, the CoNC-5 was obtained.

The commercial carbon black of Vulcan XC-72 was pre-oxidized by concentrated nitric acid at 80 °C for 10 h with magnetic stirring. Then, 100 mg of pre-oxidized XC-72 was added to the mixed solution of 10 mL of ultra-pure water and 10 mL of ethanol. After ultrasonic dispersion for 30 min, 2 mL of $Co(NO_3)_2{\cdot}6H_2O$ solution (with 2 wt.% Co content) was added under an ultrasonic environment for 1 h. Subsequently, 1 g of dicyandiamide and dried precursor were respectively placed upstream and downstream of the Ar flow with a flow rate of 100 mL·min^{-1} in the tube furnace, and heated to 800 °C at 5 °C·min^{-1} for 1 h. After pickling, washing, and drying, the CoNC-6 was obtained.

2.3 Preparation of oxygen-functionalized CoNC catalysts

The O-CoNC was obtained using a commercial 30 wt.% H_2O_2 solution as an oxidizing agent in an acidic medium. Specifically, 50 mg of CoNC catalyst was dispersed in 50 mL of 0.5 M H_2SO_4 and heated to 90 °C. Then, 5 mL of 30 wt.% H_2O_2 solution was gradually added to the above mixture every 20 min for 2 h. The

content of H_2O_2 in the reaction solution was 11 wt.%. Finally, the O-CoNC (also named O-CoNC(11) and O-CoNC(H_2O_2)) catalysts were collected by filtration, rinsed with deionized (DI) water, and dried overnight in a vacuum oven at 60 °C.

The CoNC-*X* (*X* = 1–6) catalyst prepared using different methods was also functionalized under the same conditions to prepare the O-CoNC-*X* (*X* = 1–6) sample.

To explore the effect of oxidation degree on the structure and property of the catalysts, O-CoNC-*Y* (*Y* = 3 wt.% and 6 wt.% of H_2O_2) catalysts were prepared under the same conditions of O-CoNC, except for adding 1 and 2 mL of 30 wt.% H_2O_2 solution every 20 min for 2 h, respectively.

50 mg of CoNC catalyst was dispersed in 30 mL of concentrated nitric acid solution and heated to 50 °C for 6 h. The treated samples were collected by filtration, rinsed with deionized water, and dried overnight in a vacuum oven at 60 °C to obtain the O-CoNC(HNO_3) catalysts.

100 mg of CoNC catalyst was heated to 200 °C at 5 °C·min^{-1} for 1 h in an air atmosphere to obtain the O-CoNC(air) catalysts.

2.4 Preparation of reduced CoNC catalysts

50 mg of O-CoNC sample was heated to 300 °C at 2 °C·min^{-1} in an Ar/H_2 (10 vol.%) atmosphere with a flow rate of 100 mL·min^{-1} for 1 h to obtain the R-CoNC catalysts.

2.5 Preparation of single-atom dispersed CoNC catalysts

The single-atom dispersed CoNC, denoted as SA-CoNC, was obtained by the same conditions as CoNC, except for pyrolyzed under a 10 vol.% H_2/Ar atmosphere [41].

2.6 Electrochemical measurements

The ORR polarization curves of all catalysts were tested by a typical three-electrode method with a rotating ring-disk electrode as the working electrode, and the collection coefficient was corrected to 0.37, as shown in Fig. S1 in the ESM.

3 Results and discussion

Figure 1 briefly illustrates the preparation procedure of CoNC and O-CoNC catalysts. The pristine CoNC catalyst (denoted as CoNC) was prepared by the pyrolysis of 2-methylimidazole cobalt salt (ZIF-67), followed by acid treatment to remove the impurities and residual metal species. The CoNC was then subjected to a certain concentration of H_2O_2 solution (11 wt.%) and heat-treated at a temperature of 90 °C for 2 h. After cooling and washing with DI water, the oxygen-functionalized CoNC catalyst (marked as O-CoNC) was obtained.

The morphologies of CoNC and O-CoNC samples were investigated by scanning electron microscopy (SEM) and transmission electron microscopy (TEM) techniques. The SEM images in Fig. S2 in the ESM reveal that the two samples almost keep the same morphology as the typical ZIF-67 frameworks. Notably, despite the catalyst being subjected to acid washing during the preparation process to remove unstable impurities and cobalt nanoparticles as much as possible, the TEM images in Fig. 2(a) and Fig. S3 in the ESM reveal that CoNC contains obvious metal nanoparticles ranging from a few to tens of nanometers. This can be attributed to the catalytic effect of Co on the graphitization of the carbon under high-temperature conditions, and some cobalt nanoparticles are encapsulated by the carbon layer, as shown in Fig. S4 in the ESM [20, 41, 42]. In contrast, no obvious metal nanoparticles are observed in O-CoNC (Fig. 2(b) and Fig. S5 in the ESM). The high-angle annular dark-field scanning transmission electron microscopy (HAADF-STEM) images and energy-dispersive X-ray spectroscopy (EDS) mapping results in Fig. S6 in the ESM further reveal that the O-CoNC exhibits significantly fewer aggregated Co particles compared to CoNC. This indicates that the oxidation treatment facilitates the elimination of Co nanoparticles. Notably, the inductively coupled plasma mass spectrometry (ICP-MS) results in Table S2 in the ESM show that the Co content of O-CoNC (4.3 wt.%) is slightly lower than that of CoNC (5.1 wt.%), suggesting that a small amount of Co dissolves during the oxidation treatment, but most remains in the catalysts. Their X-ray diffraction (XRD) patterns in Fig. S7 in the ESM show two broad peaks around 26° and 43°, corresponding to the (002) and (100) lattice of graphitic carbon, respectively. In addition, two metallic Co diffraction peaks at 44.2° and 51.5° are also observed, where the CoNC shows a stronger intensity of Co(111) plane (0.43 normalized to the C(002) peak) compared to O-CoNC (0.25 normalized to the C(002) peak), indicating a stronger crystallinity of metallic Co, in great consistent with the above TEM result. Our previous works have demonstrated that the elimination of metal nanoparticles in CoNC catalysts enhances their selectivity for H_2O_2 production [20, 41, 42].

Raman spectra were performed to investigate the defect information of the catalysts. As shown in Fig. S8 in the ESM, both CoNC and O-CoNC contain two broad bands near 1350 and 1600 cm^{-1}, corresponding to the defects (D band) and the graphitic

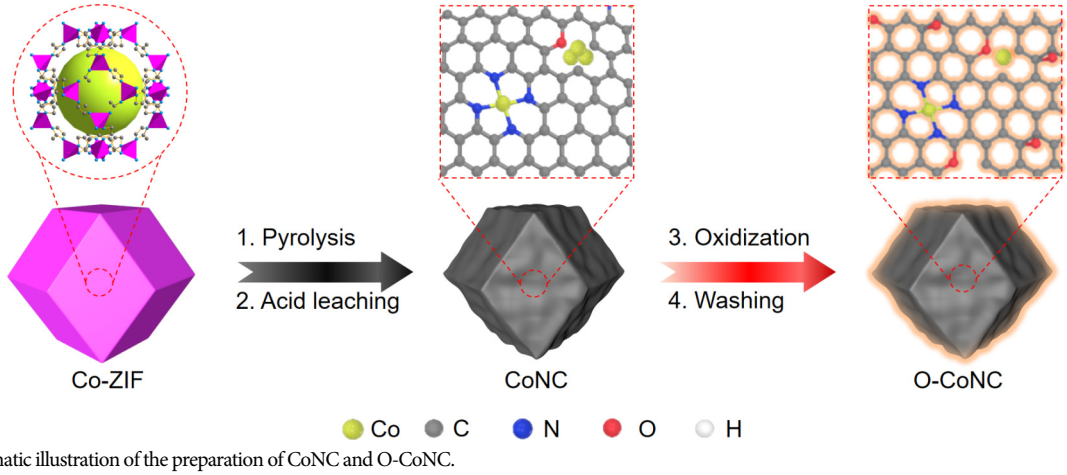

Figure 1 Schematic illustration of the preparation of CoNC and O-CoNC.

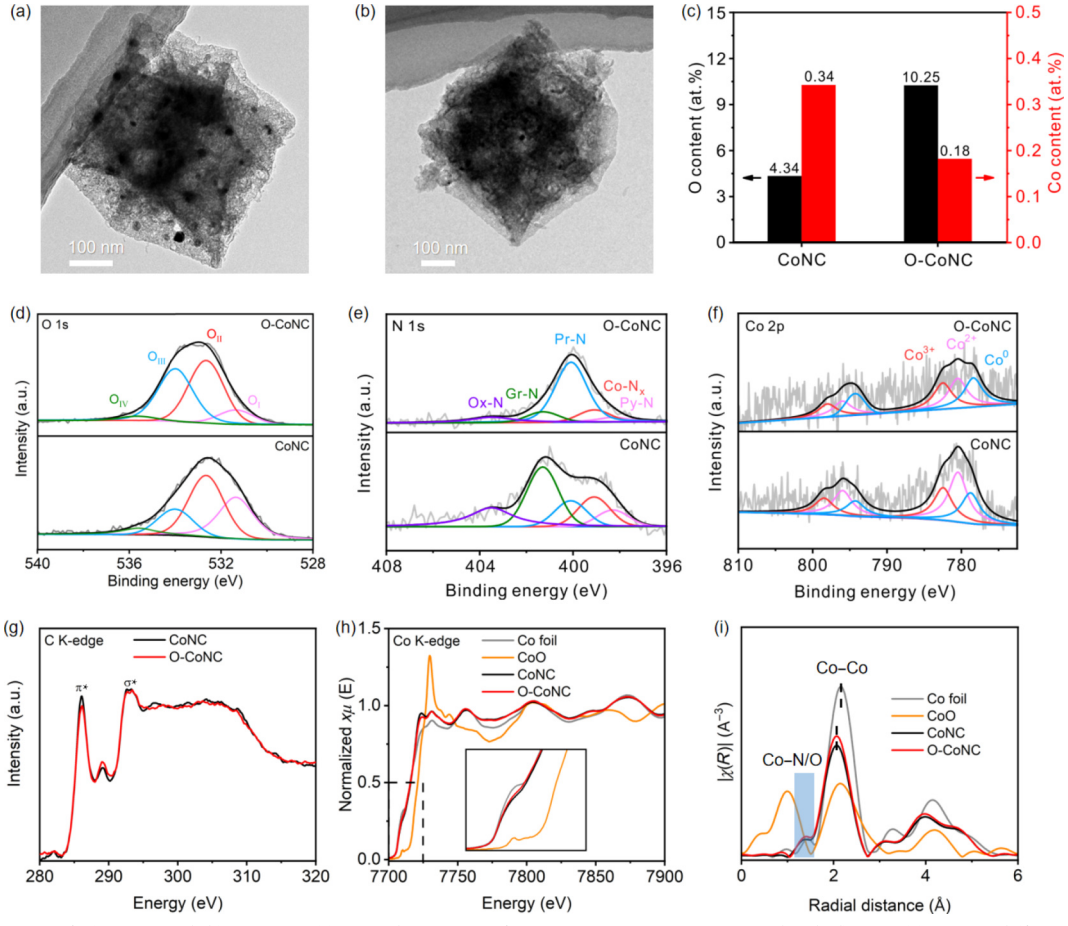

Figure 2 TEM images of (a) CoNC and (b) O-CoNC. (c) Co and O contents from XPS survey spectra. Deconvoluted (d) O 1s, (e) N 1s, and (f) Co 2p. (g) C K-edge NEXAFS spectra of CoNC and O-CoNC catalyst. (h) Co K-edge NEXAFS and (i) FT-EXAFS spectra of Co foil, CoO, CoNC, and O-CoNC in *R* space.

lattice (G band) of carbon, respectively. The calculated intensity ratio of the D band and G band (I_D/I_G) is 1.01 for CoNC and 1.02 for O-CoNC, indicating a similar defect degree [44–46]. To further probe the principal types of defects in the catalysts, the Raman spectra were deconvoluted into five bands near 1200, 1350, 1500, 1580, and 1620 cm^{-1}, corresponding to the polyene, graphene edges, amorphous, graphite lattice, and graphene layers, respectively [47]. The fitting results in Table S3 in the ESM reveal that the O-CoNC contains almost the same content as the CoNC, except for a slightly decreased D4 band and increased D1 band. This indicates that the oxidation treatment contributes to the transformation of polyene to graphene edges of the carbon matrix, and the graphene edges are reported to be intrinsically selective for $2e^-$ ORR.

The surface state and chemical environment of the catalysts were investigated via Fourier transform infrared (FTIR), X-ray photoelectron spectroscopy (XPS), near-edge X-ray absorption fine structure (NEXAFS), and Fourier transform extended X-ray absorption fine structure (FT-EXAFS). As shown in the FTIR spectra (Fig. S9 in the ESM), the four main oxygenated groups can be assigned to stretching vibration of hydroxyl (υ(OH)) at 3440 cm^{-1}, stretching vibration of ketones (υ(C=O)) at 1700 cm^{-1}, deformation vibration of hydroxyl (δ(OH)) at 1380 cm^{-1}, and asymmetric stretching vibration of ethers (υ(C–O–C)) at 1057 cm^{-1} [47–49]. The O-CoNC has a relatively higher intensity of peaks compared to CoNC, which may indicate a higher content of oxygen functional groups. This is further supported by the XPS results. Fig. S10 in the ESM shows peaks around 284.8, 400.8, 532.7, and 782.8 eV, corresponding to C 1s, N 1s, O 1s, and Co 2p, respectively. The XPS survey spectra reveal that the surface O content increases from 4.34 at.% for CoNC to 10.25 at.% for O-CoNC, and the surface Co content decreases from 0.34 at.% for CoNC to 0.18 at.% for O-CoNC (Fig. 2(c) and Table S4 in the ESM), suggesting that OFGs cover the catalysts surface, thereby reducing the relative content of Co. The O 1s spectra were further deconvoluted into O_I (C=O related groups) at 531.35 eV, O_{II} (C–O–C or COOH) at 532.8 eV, O_{III} (C–O(H)) at 534.0 eV, and O_{IV} (physically adsorbed H_2O and O_2) at 535.6 eV [47–49]. The fitting results in Fig. 2(d) and Table S5 in the ESM reveal that the content of O_I decreased and O_{III} increased significantly after the oxidation treatment, suggesting the decrease of C=O related groups and increase of C–O(H) groups, which can cause the deeper coverage of OFGs owing to the longer bond length. In addition, the N 1s spectra were deconvoluted into pyridinic-N (Py-N) at 398.3 eV, Co-N_x at 399.1 eV, pyrrolic-N (Pr-N) at 400.1 eV, graphitic-N (Gr-N) at 401.3 eV, and oxidized-N (Ox-N) at 403.5 eV [4, 5, 24, 41, 50]. The fitting results in Fig. 2(e) and Table S6 in the ESM reveal that the content of Gr-N decreased and Pr-N increased significantly after the oxidation treatment. This may be attributed to the reactive oxygen species (such as hydroxyl radical) generated during the oxidation treatment that cleave partially unstable bonds (such as Gr-N with weak coordination to Co) [47]. The Pr-N coordinated Co site was reported to be mainly responsible for $2e^-$ ORR [16]. Moreover, the Co 2p spectra were deconvoluted into Co^0 (778.8 and 794.3 eV), Co^{2+} (780.5 and 796.0 eV), and Co^{3+} (782.5

and 798.0 eV) [4, 24, 41]. The fitting results in Fig. 2(f) and Table S7 in the ESM reveal that the atomic content of all types of Co species in CoNC decreases after oxidation. This phenomenon can be attributed to the enrichment of oxygen species on the catalyst surface, which leads to the coverage of Co active sites. The C K-edge NEXAFS spectra (Fig. 2(g)) reveal unoccupied π* and σ* states, with the peaks around 286, 288.5, and 292.5 eV corresponding to π* (C=C), π* (C=O), and σ* (C–C) transitions, respectively [5]. The intensity of the π* (C=O) increased significantly after the oxidation treatment, indicating a higher C=O content in O-CoNC compared to CoNC, which is in great consistency with the XPS results. The Co K-edge NEXAFS spectra (Fig. 2(h)) show that the absorption edge positions of CoNC and O-CoNC are nearly identical, with both located between those of Co foil (metallic Co^0 reference) and CoO (oxidized Co^{2+} reference), suggesting their partially oxidized state [4, 41]. The FT-EXAFS spectra in *R* space (Fig. 2(i)) provide further insight into the local coordination environment of cobalt in the samples. The Co foil exhibits a prominent second-shell peak around 2.2 Å. In contrast, both CoNC and O-CoNC display a single dominant peak around 2 Å, which is negatively shifted relative to the typical Co–Co bond distance. This observation indicates that partial cobalt is coordinated mainly with light atoms such as N or O [4, 26, 41]. Notably, the amplitude of the dominant peak around 2 Å in O-CoNC is slightly higher than that in CoNC, suggesting an enhancement in coordination strength. Additionally, the shoulder peak around 1.4 Å (corresponding to Co–N/O coordination) in O-CoNC is stronger than that in CoNC, further confirming the enhanced coordination environment [16].

To further describe the variation of electrochemical performance of the samples with or without oxidation treatment, the pristine CoNC catalyst was also oxidized at the H_2O_2 with different concentrations of 3 wt.%, 6 wt.%, and 11 wt.%, which were labeled as O-CoNC(*Y*) (*Y* = 3 wt.%, 6 wt.%, and 11 wt.% of H_2O_2). The XRD, Raman, FTIR, and XPS characterization results in Fig. S11 in the ESM further confirm that the H_2O_2 oxidation treatment has little effect on the structure of the catalysts, but can significantly increase the content of oxygen species on the surface. As shown in Fig. 3(a), compared to pristine CoNC, all the O-CoNC catalysts reveal increased ring current densities, but decreased E_0 values and disk current densities. With the increase of oxidation degree, the H_2O_2 selectivity (Fig. S12 in the ESM) increases, but the ORR activity (E_0, defined as the potential vs. reversible hydrogen electrode (RHE) for 0.1 mA·cm^{-2} by subtracting the N_2 current density from the O_2 current density) decreases (Fig. 3(b)). The RRDE-observed results demonstrate that the introduction of oxygenated groups can indeed improve the H_2O_2 selectivity of CoNC catalysts. Combined with the above characteristic results, the increased H_2O_2 selectivity can be attributed to the elimination of Co nanoparticles and the increased Pr-N content, while the decreased ORR activity may be related to the coverage of OFGs and the decline of Co content on the surfaces.

As for GDE measurements, the CoNC electrode shows a much higher O_2 reduction polarization current density than O-CoNC electrodes (Fig. 3(c)). The current density of the CoNC electrode in chronoamperometry testing is almost double that of O-CoNC electrodes (inset of Fig. 3(c)). After collecting the electrolytes and measuring via the cerium sulfate titration method, the generated H_2O_2 can be quantified, and correspondingly, the H_2O_2 yield rate and Faraday efficiency values of the electrodes are obtained (Fig. 3(d)). Compared with those of O-CoNC(*Y*) catalyst (274 to 362 mg·L^{-1}·h^{-1}) electrodes, the CoNC electrode shows a much higher H_2O_2 yield rate of 542 mg·L^{-1}·h^{-1}, but its Faraday efficiency (61.8%) is only slightly lower compared with the O-CoNC (73.4%). The GDE-observed results demonstrate that the introduction of oxygenated groups into CoNC catalysts is not in favor of the H_2O_2 synthesis in actual conditions, on the contrary, it will lead to a lower H_2O_2 yield. Considering that the H-cell utilizes the dissolved O_2, rather than the gaseous O_2, as the reactant, the flow-cell was assembled to construct the three-phase interface. As shown in Fig. S13 in the ESM, the flow cell shows the same trend as the H-cell results, in which the Faraday efficiency increases slightly but the

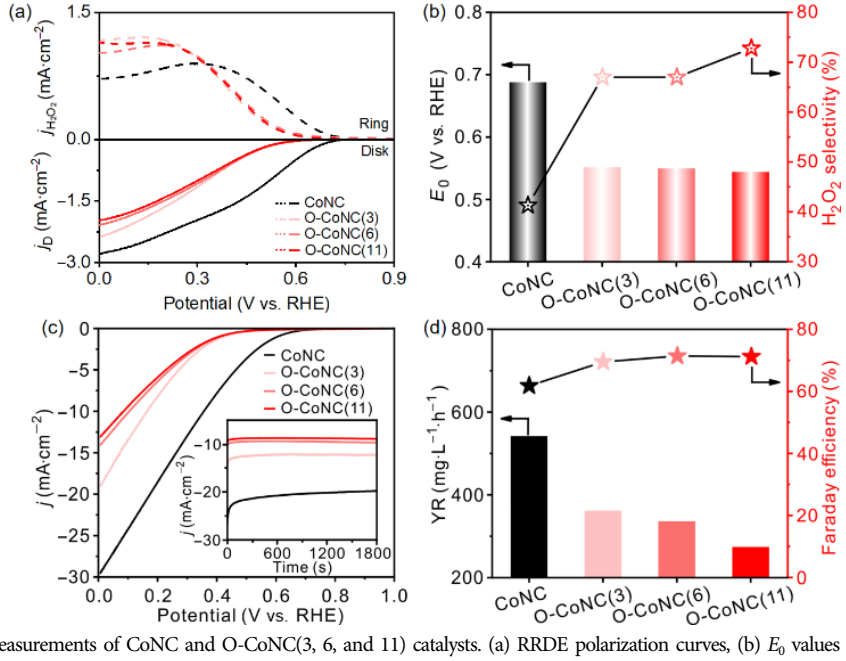

Figure 3 RRDE and GDE measurements of CoNC and O-CoNC(3, 6, and 11) catalysts. (a) RRDE polarization curves, (b) E_0 values and the H_2O_2 selectivity of the catalysts calculated from RRDE, (c) GDE polarization curves, the inset showing chronoamperometry curves at a potential of 0.1 V vs. RHE, and (d) their detected H_2O_2 YR and Faraday efficiency of the CoNC and O-CoNC(3, 6, and 11) catalysts in 0.1 M $HClO_4$.

H_2O_2 yield rate decreases sharply with the increased oxidizing concentration.

For comparison, we prepared a single-atom dispersed CoNC catalyst (denoted as SA-CoNC) under the same conditions as CoNC, except for pyrolyzed under a 10 vol.% H_2/Ar atmosphere [41]. The SEM, TEM, and high-resolution TEM (HR-TEM) images in Fig. S14 in the ESM reveal that the SA-CoNC exhibits a dodecahedral morphology assembled from nanotubes, with no metallic particles observed. The ICP-MS results in Table S2 in the ESM indicate that the Co content of SA-CoNC is less than half that of CoNC and O-CoNC. Electrochemical tests (Fig. S15 in the ESM) reveal that SA-CoNC exhibits both higher RRDE and GDE performance than CoNC and O-CoNC, demonstrating that Co-N_x sites are the core active centers. In contrast, the presence of cobalt nanoparticles not only reduces the utilization efficiency of active sites but also facilitates the decomposition of H_2O_2.

To further confirm the differences between RRDE and GDE measurements, the CoNC material was also subjected to concentrated HNO_3 or air oxidation treatment to obtain the samples of O-CoNC(HNO_3) and O-CoNC(air), respectively. The XRD, Raman, FTIR, and XPS results in Fig. S16 in the ESM reveal that the catalysts prepared by different procedures possess different characteristics. For example, the O-CoNC(HNO_3) has a significant σ OH in FTIR, while O-CoNC(air) has the lowest signal. To further elucidate the effects of different OFGs on the performance of CoNC, the O 1s XPS spectra of the catalysts are analyzed. The fitting results in Fig. S17 and Table S5 in the ESM reveal that the O_{III} content of O-CoNC(H_2O_2), O-CoNC(HNO_3), and O-CoNC(air) decreases sequentially. Despite the structural differences, the catalysts oxidized by various methods display the same trend in terms of electrocatalytic performance. As exhibited in Figs. 4(a) and 4(b), and Fig. S18 in the ESM, from RRDE measurements, both O-CoNC(HNO_3) and O-CoNC(air) samples show higher H_2O_2 selectivity values (80.6% and 70.5%, respectively) but lower ORR onset potentials (0.625 and 0.612 V, respectively) in comparison with pristine CoNC (E_0 = 0.688 V, H_2O_2 selectivity = 41.3%). While for GDE shown in Figs. 4(c) and 4(d), the CoNC electrode still possesses a much higher H_2O_2 production rate, along with a relatively lower Faraday efficiency value than O-CoNC(HNO_3) and O-CoNC(air) samples. Notably, the H_2O_2 production rates of O-CoNC(H_2O_2), O-CoNC(HNO_3), and O-CoNC(air) increase sequentially, which is exactly opposite to the trend of their O_{III} group content. This indicates that the introduction of C–O(H) functional groups on the surface of CoNC catalysts is unfavorable for the electrochemical synthesis of H_2O_2.

In addition, to confirm the universality of this phenomenon, we also prepared six other types of CoNC catalysts by using different precursors and procedures (detailed in Table S8 in the ESM), which are labeled as CoNC-*X* (*X* = 1–6), respectively. After the oxidation by H_2O_2 treatment, the corresponding samples are marked as O-CoNC-*X*. Interestingly and remarkably, as displayed in Fig. 5 and Figs. S19–S26 in the ESM, these CoNC-*X* samples and the corresponding O-CoNC-*X* samples also follow the same trend as the above results. The CoNC-*X* samples reveal a much higher E_0 and production rate with relatively lower H_2O_2 selectivity and Faraday efficiency values than the corresponding O-CoNC-*X* samples. All of the evidence reveals that the introduction of oxygenated groups into CoNC catalysts is not in favor of improving the H_2O_2 electrosynthesis performance, on the contrary, it will lead to a sharp decline in the productivity of H_2O_2.

Based on the above results and discussion, we propose a mechanism by which OFGs influence the H_2O_2 electrosynthesis performance of the CoNC catalyst. One is that the oxidation treatment changes the intrinsic properties of the catalyst. Specifically, the oxidizing treatment eliminates the Co nanoparticles (as evidenced by the TEM results in Figs. 2(a) and 2(b), and Figs. S3–S6 in the ESM) and modulates the surface chemical environment of CoNC (as shown in XPS results in Figs. 2(c)–2(f)). This contributes to the enhancement of 2e⁻ selectivity. Moreover, the oxidizing treatment increases the coverage of OFGs on the

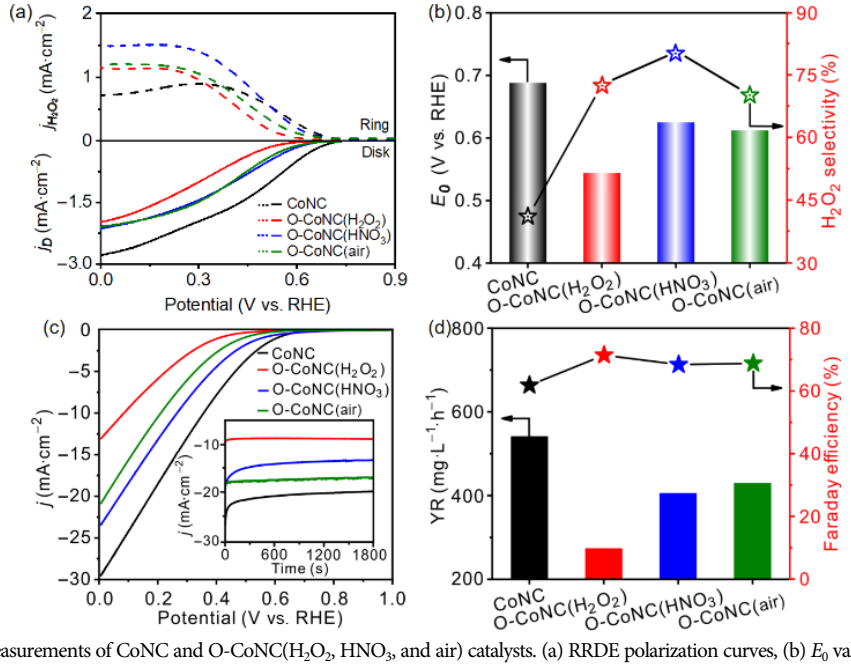

Figure 4 RRDE and GDE measurements of CoNC and O-CoNC(H_2O_2, HNO_3, and air) catalysts. (a) RRDE polarization curves, (b) E_0 values and the H_2O_2 selectivity of the catalysts calculated from RRDE, (c) GDE polarization curves, the inset showing chronoamperometry curves at a potential of 0.1 V vs. RHE, and (d) their detected YR and Faraday efficiency of the CoNC and O-CoNC(H_2O_2, HNO_3, and air) catalysts in 0.1 M $HClO_4$.

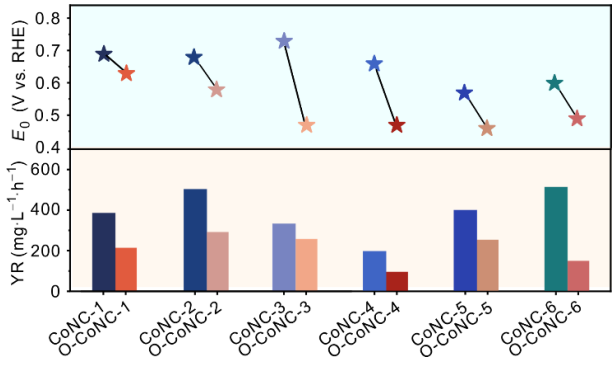

Figure 5 The comparative results of RRDE and GDE measurements of the CoNC-*X* and O-CoNC-*X* catalysts, as obtained from Figs. S19–S24 in the ESM and detailed in Table S9 in the ESM.

catalyst surface, hence reducing the relative surface content of Co species, leading to an attenuation in ORR activity. The second and most important point is ascribed to the microenvironment of the catalytic interface. When the catalyst is oxidized, the surface will become hydrophilic and gas-phobic, which greatly hinders the mass transfer of O_2 to the catalytic interface [51–53], leading to low H_2O_2 yield (see below).

To confirm the above conjecture, we subjected the O-CoNC sample to H_2 reduction treatment at 300 °C to remove the oxygenated groups. The as-obtained material is named R-CoNC. Fig. 6(a) illustrates the schematic diagram of CoNC, O-CoNC, and R-CoNC samples. The SEM and TEM images in Fig. S27 in the ESM reveal that the R-CoNC possesses the same typical ZIF-67 framework with minor metal nanoparticles, similar to O-CoNC. This indicates that the reduction treatment has scarcely altered the structural characteristics of the O-CoNC sample, as proved by the XRD, Raman, NEXAFS, and FT-EXAFS results. The XRD patterns in Fig. S28 in the ESM show that the intensity of the Co (111) plane for R-CoNC (0.28) is comparable to that of O-CoNC (0.25), while both are much lower than that of CoNC (0.43), indicating that the Co species of R-CoNC remain in an atomic dispersion state. The Raman spectra in Fig. S29 in the ESM and fitting results in Table S3 in the ESM demonstrate that the defect degree and content of R-CoNC are highly similar to those of O-CoNC, with slight differences from CoNC (as previously discussed). The C K-edge NEXAFS spectra in Fig. S30 in the ESM show that the intensities of π^* (C=C) and π^* (C=O) transitions in R-CoNC are reduced compared to those in O-CoNC, which can be attributed to the introduction of defect sites resulting from the removal of OFGs. The Co K-edge NEXAFS spectra (Fig. S31 in the ESM) and FT-EXAFS in *R* space (Fig. S32 in the ESM) exhibit that the edge position and peaks of R-CoNC are nearly identical to those of O-CoNC, with only a slight shift toward the CoNC direction. These results suggest that the atomic dispersion and coordination state of cobalt in R-CoNC are minimally affected by the reduction treatment and remain essentially consistent with those in O-CoNC. On the contrary, the FTIR and XPS results (Figs. 6(b)–6(d), and Figs. S33 and S34 and Tables S4–S7 in the ESM) reveal that the type and content of surface states for R-CoNC are restored almost to the same level as pristine CoNC, suggesting that the effects of OFGs on the chemical environment of CoNC catalysts can be recovered after appropriate reduction treatment. Notably, the ICP-MS results in Table S2 in the ESM show that the Co content of R-CoNC (4.0 wt.%) is even slightly lower than that of O-CoNC (4.3 wt.%), while the XPS results of the R-CoNC (0.35 at.%) indicate that its surface Co content is even higher than that of CoNC (0.34 at.%). Considering that XPS is a surface-sensitive analytical technique that primarily probes the information from the top few atomic layers, these results suggest that the coverage and removal of OFGs significantly influence the surface chemical state of the catalysts. Given that electrocatalytic reactions are inherently surface-based processes, the surface state of the catalysts plays a crucial role in determining their performance. As a result, the electrocatalytic performance (Fig. S35 in the ESM) of R-CoNC recovers or even enhances to a higher level than CoNC. Impressively, the ORR activity (E_0 and H_2O_2 yield rate) and selectivity (H_2O_2 selectivity and Faraday efficiency) of the catalysts exhibit the same trends as their Co and O content on the surface (Figs. 6(e)–6(g)), respectively, indicating the strong correlation between the $2e^-$ ORR performance and its surface chemical states. Regarding long-term operational stability, the O-CoNC exhibited a more significant degradation than CoNC and R-CoNC during the cyclic stability tests, indicating inferior stability (Fig. S36 in the ESM). Notably, the H_2O_2 yield rate remained nearly unchanged within each cycle but declined substantially when reused in subsequent cycles. This indicates that the active sites of the catalyst did not undergo significant dissolution or corrosion, but rather points to the mass transfer-limited degradation induced by electrode flooding.

When it comes to the reaction interface, the introduction of OFGs affects the wetting characteristics of the catalysts, thus influencing the performance of H_2O_2 electrosynthesis. In general, most oxygen-containing functional groups are hydrophilic. As a result, the O-CoNC powder is easily dispersed in the electrolyte due to the surface hydrophilicity and wettability, while the corresponding CoNC and R-CoNC powder are suspended on the electrolyte surface (left side of Fig. 6(h)). The contact angle value decreases after oxidation and then increases with H_2 reduction treatment, meaning that the surface of the catalysts goes from hydrophobic to hydrophilic, and then from hydrophilic to hydrophobic, which is in good consistency with the change of surface oxygen content (first increases and then decreases). As reported, hydrophobic interfaces promote O_2 diffusion efficiency [54, 55]. The bubble contact images in Fig. S37 in the ESM confirm that the O-CoNC shows a much slower bubble adsorption rate as compared to CoNC and R-CoNC. Accordingly, a schematic diagram depicting the surface structural evolution of the CoNC, O-CoNC, and R-CoNC catalysts and corresponding changes in electrochemical oxygen reduction behavior is provided in Fig. 6(i). The introduction of OFGs into the CoNC catalyst will cover the Co-active sites and cause the surface to be hydrophilic (forming a water layer that acts as a mass transport barrier for hydrophobic O_2), leading to the decline of H_2O_2 production. To further verify this mechanism and investigate the effect of specific OFGs types on the hydrophobicity of the material, the contact angles of O-CoNC(HNO_3) and O-CoNC(air) were also measured. As shown in Fig. S38 in the ESM, the contact angle values of O-CoNC(air) are higher than that of O-CoNC(HNO_3), suggesting the enhanced hydrophobicity. This trend is opposite to the content of O_{III} in the materials. As shown in Fig. S39 in the ESM, we further found that the contact angle of the catalyst is inversely proportional to the O_{III} content of the as-prepared catalysts. Overall, we demonstrated that the introduction of OFGs into CoNC catalysts is not conducive to the electrosynthesis of H_2O_2 in practice, on the contrary, it appears to be detrimental.

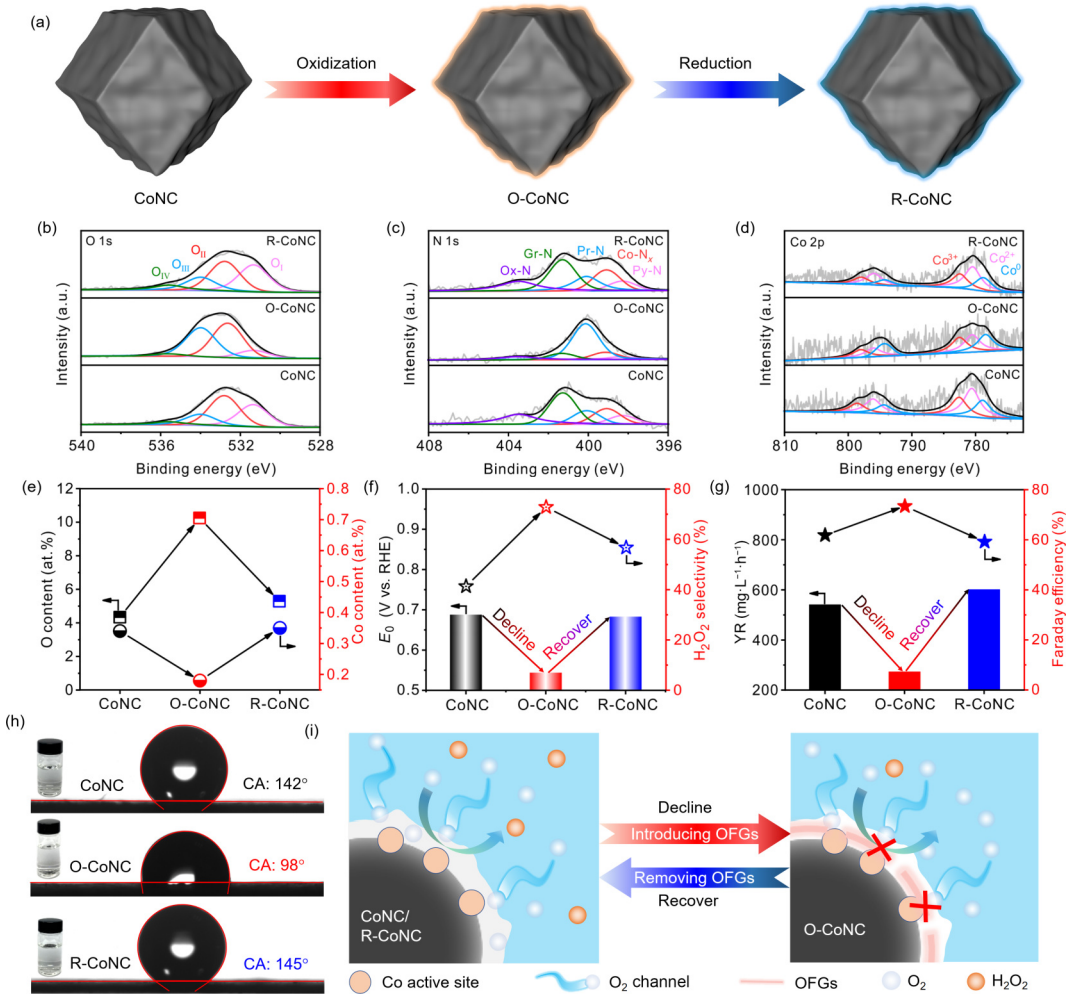

Figure 6 Mechanism investigation and demonstration. (a) Sketch map of the evolution. Deconvoluted (b) O 1s, (c) N 1s, and (d) Co 2p spectra. (e) Co and O contents and ((f) and (g)) RRDE and GDE measurements as derived from Fig. S35 in the ESM. (h) Contact angles. (i) Schematic diagram of the oxygen reduction behaviors on the CoNC, O-CoNC, and R-CoNC catalysts.

4 Conclusions

In this work, we investigated the roles and effects of introducing OFGs into a CoNC catalyst for H_2O_2 electrosynthesis. Specifically, the oxidizing treatment promotes the atomic dispersion of Co species, the coverage of OFGs on the surface, and the regulation of coordination environments, resulting in increased 2e$^-$ selectivity but decreased ORR activity. Moreover, the introduction of OFGs enhances the hydrophilicity of the reaction interface and hinders the O_2 diffusion. Under practical conditions, this modification counterintuitively leads to a significant decrease in H_2O_2 yield. Impressively, when the surface OFGs are removed, the H_2O_2 production capability of the catalysts can be recovered and even improved. Our finding implies that future carbon-based catalyst design for H_2O_2 electrosynthesis may move beyond blind introduction of OFGs, optimizing their type, density, and distribution to balance their promotional effects (e.g., regulating surface properties) and inhibitory impacts (e.g., hindering O_2 access via hydrophilicity effects), thereby tailoring the catalyst surface properties for efficient H_2O_2 electrosynthesis. We are confident that these crucial insights will be very helpful for the development of highly efficient catalysts for sustainable H_2O_2 electrosynthesis and related fields.

Electronic Supplementary Material: Supplementary material (experimental sections, figures, and tables) is available in the online version of this article at https://doi.org/10.26599/NR.2026.94908416.

Data availability

All data needed to support the conclusions in the paper are presented in the manuscript and the Electronic Supplementary Material. Additional data related to this paper may be requested from the corresponding author upon request.

Acknowledgements

This work was supported by the National Key Research and Development Program of China (No. 2022YFA1504703), the National Natural Science Foundation of China (Nos. 22575072, 22375067, 92261204, and 22431005), the Innovational Fund for Scientific and Technological Personnel of Hainan Province (No. KJRC2023C10), the Natural Science Foundation of Hainan University (No. KYQD(ZR)23137), and Princess Nourah bint Abdulrahman University Researchers Supporting Project number (No. PNURSP2026R398), Princess Nourah bint Abdulrahman

University, Riyadh, Saudi Arabia. The authors thank the Analytical and Testing Center of Huazhong University of Science and Technology and Hainan University for related tests, the staff of Beamline BL14W at the Shanghai Synchrotron Radiation Facility (SSRF), and the Beamlines MCD-A and MCD-B (Soochow Beamline for Energy Materials) at the National Synchrotron Radiation Laboratory (NSRL) for the XAFS measurements. We also thank the Shiyanjia Lab (www.shiyanjia.com) for the XPS analysis.

Declaration of competing interest

All the contributing authors report no conflict of interests in this work.

Author contribution statement

C. Z.: Conceptualization, methodology, investigation, formal analysis, data curation, writing - original draft. H. S. H.: Methodology, investigation, formal analysis, data curation, writing – original draft. W. L.: Investigation, data curation, visualization. H. Y. Q.: Investigation, formal analysis. L. L. Z.: Investigation, validation. M. A.: Investigation, funding acquisition. L. L.: Investigation, funding acquisition. L. P. B.: Investigation, funding acquisition. G. L. H.: Investigation, funding acquisition. J. Z.: Supervision, writing – review & editing, project administration, funding acquisition. X. L.: Supervision, writing – review & editing, project administration, funding acquisition. All the authors have approved the final manuscript.

Use of AI statement

None.

References

[1] Siahrostami, S.; Verdaguer-Casadevall, A.; Karamad, M.; Deiana, D.; Malacrida, P.; Wickman, B.; Escudero-Escribano, M.; Paoli, E. A.; Frydendal, R.; Hansen, T. W. et al. Enabling direct H_2O_2 production through rational electrocatalyst design. *Nat. Mater.* **2013**, *12*, 1137–1143.

[2] Lu, Z. Y.; Chen, G. X.; Siahrostami, S.; Chen, Z. H.; Liu, K.; Xie, J.; Liao, L.; Wu, T.; Lin, D. C.; Liu, Y. Y. et al. High-efficiency oxygen reduction to hydrogen peroxide catalysed by oxidized carbon materials. *Nat. Catal.* **2018**, *1*, 156–162.

[3] Sheng, H. Y.; Hermes, E. D.; Yang, X. H.; Ying, D. W.; Janes, A. N.; Li, W. J.; Schmidt, J. R.; Jin, S. Electrocatalytic production of H_2O_2 by selective oxygen reduction using earth-abundant cobalt pyrite (CoS_2). *ACS Catal.* **2019**, *9*, 8433–8442.

[4] Jung, E.; Shin, H.; Lee, B. H.; Efremov, V.; Lee, S.; Lee, H. S.; Kim, J.; Hooch Antink, W.; Park, S.; Lee, K. S. et al. Atomic-level tuning of Co-N-C catalyst for high-performance electrochemical H_2O_2 production. *Nat. Mater.* **2020**, *19*, 436–442.

[5] Zhang, C.; Shen, W. Q.; Guo, K.; Xiong, M.; Zhang, J.; Lu, X. A pentagonal defect-rich metal-free carbon electrocatalyst for boosting acidic O_2 reduction to H_2O_2 production. *J. Am. Chem. Soc.* **2023**, *145*, 11589–11598.

[6] Shen, W. Q.; Zhang, C.; Alomar, M.; Du, Z. L.; Yang, Z. P.; Wang, J. J.; Xu, G. Q.; Zhang, J.; Lv, J.; Lu, X. Fullerene-derived boron-doped defective nanocarbon for highly selective H_2O_2 electrosynthesis. *Nano Res.* **2024**, *17*, 1217–1224.

[7] Shen, W. Q.; Zhang, C.; Wang, X. Y.; Huang, Y. Z.; Du, Z. L.; Alomar, M.; Wang, J. J.; Lv, J.; Zhang, J.; Lu, X. Sulfur-doped defective nanocarbons derived from fullerenes as electrocatalysts for efficient and selective H_2O_2 electroproduction. *ACS Materials Lett.* **2024**, *6*, 17–26.

[8] Li, F. X.; Qin, N.; Zhang, H. F.; Zhang, C.; Alomar, M.; Bao, L. P.; Zhao, S. Q.; Zhang, J.; Lu, X. Engineering carbonaceous materials for electrochemical four-electron and two-electron oxygen reduction reactions. *Renewables* **2025**, *3*, 2–20.

[9] Zhang, C.; He, C. L.; Zhang, J.; Lu, X. Hydrogen peroxide electrosynthesis from seawater. *SmartMat* **2025**, *6*, e70035.

[10] Huang, X.; Song, M.; Zhang, J. J.; Shen, T.; Luo, G. Y.; Wang, D. L. Recent advances of electrocatalyst and cell design for hydrogen peroxide production. *Nano-Micro Lett.* **2023**, *15*, 86.

[11] Guo, W. J.; Wang, Y. W.; Shen, S. Y.; Wang, H.; Shao, K.; Wang, Z. J.; Shi, Y. R.; Li, C. C.; Sun, Q. F.; Li, H. Q. Wood-inspired electrode for sustainable electrocatalytic energy conversion. *SmartMat* **2025**, *6*, e1326.

[12] Sun, D. D.; Sun, Z. P.; Yang, D. H.; Jiang, X. F.; Tang, J.; Wang, X. B. Advances in boron nitride-based materials for electrochemical energy storage and conversion. *EcoEnergy* **2023**, *1*, 375–404.

[13] Zheng, R. X.; Meng, Q. L.; Zhang, L.; Ge, J. J.; Liu, C. P.; Xing, W.; Xiao, M. L. Co-based catalysts for selective H_2O_2 electroproduction via 2-electron oxygen reduction reaction. *Chem.—Eur. J.* **2023**, *29*, e202203180.

[14] Zhao, X.; Yin, Q.; Mao, X. N.; Cheng, C.; Zhang, L.; Wang, L.; Liu, T. F.; Li, Y. Y.; Li, Y. G. Theory-guided design of hydrogen-bonded cobaltoporphyrin frameworks for highly selective electrochemical H_2O_2 production in acid. *Nat. Commun.* **2022**, *13*, 2721.

[15] Sun, Y. Y.; Silvioli, L.; Sahraie, N. R.; Ju, W.; Li, J. K.; Zitolo, A.; Li, S.; Bagger, A.; Arnarson, L.; Wang, X. L. et al. Activity–selectivity trends in the electrochemical production of hydrogen peroxide over single-site metal-nitrogen-carbon catalysts. *J. Am. Chem. Soc.* **2019**, *141*, 12372–12381.

[16] Chen, S. Y.; Luo, T.; Li, X. Q.; Chen, K. J.; Fu, J. W.; Liu, K.; Cai, C.; Wang, Q. Y.; Li, H. M.; Chen, Y. et al. Identification of the highly active Co–N_4 coordination motif for selective oxygen reduction to hydrogen peroxide. *J. Am. Chem. Soc.* **2022**, *144*, 14505–14516.

[17] Rawah, B. S.; Li, W. Z. Electrocatalytic generation of hydrogen peroxide on cobalt nanoparticles embedded in nitrogen-doped carbon. *Chin. J. Catal.* **2021**, *42*, 2296–2305.

[18] Tian, Y. H.; Li, M.; Wu, Z. Z.; Sun, Q.; Yuan, D.; Johannessen, B.; Xu, L.; Wang, Y.; Dou, Y. H.; Zhao, H. J. et al. Edge-hosted atomic Co–N_4 sites on hierarchical porous carbon for highly selective two-electron oxygen reduction reaction. *Angew. Chem., Int. Ed.* **2022**, *61*, e202213296.

[19] Wang, Y.; Zhou, Y. T.; Feng, Y.; Yu, X. Y. Synergistic electronic and pore structure modulation in open carbon nanocages enabling efficient electrocatalytic production of H_2O_2 in acidic medium. *Adv. Funct. Mater.* **2022**, *32*, 2110734.

[20] Zhang, J. J.; Liu, W.; He, F.; Song, M.; Huang, X.; Shen, T.; Li, J. W.; Zhang, C.; Zhang, J.; Wang, D. L. Highly dispersed Co atoms anchored in porous nitrogen-doped carbon for acidic H_2O_2 electrosynthesis. *Chem. Eng. J.* **2022**, *438*, 135619.

[21] Zhang, Q. R.; Tan, X.; Bedford, N. M.; Han, Z. J.; Thomsen, L.; Smith, S.; Amal, R.; Lu, X. Y. Direct insights into the role of epoxy groups on cobalt sites for acidic H_2O_2 production. *Nat. Commun.* **2020**, *11*, 4181.

[22] Liu, W. X.; Feng, J. X.; Yin, R. L.; Ni, Y. F.; Zheng, D.; Que, W. B.; Niu, X. X.; Dai, X. J.; Shi, W. H.; Wu, F. F. et al. Tailoring oxygenated groups of monolithic cobalt-nitrogen-carbon frameworks for highly efficient hydrogen peroxide production in acidic media. *Chem. Eng. J.* **2022**, *430*, 132990.

[23] Suk, M.; Chung, M. W.; Han, M. H.; Oh, H. S.; Choi, C. H. Selective H_2O_2 production on surface-oxidized metal-nitrogen-carbon electrocatalysts. *Catal. Today* **2021**, *359*, 99–105.

[24] Liu, Z. X.; Wang, D.; Zhang, M. Q.; Ma, H. C.; Wang, G. W. Highly active and selective H_2O_2 electrosynthesis in O-rich ZIF-67 derived Co-N/O-C cathode for ofloxacin oxidation. *Appl. Catal. B: Environ.* **2023**, *324*, 122252.

[25] Li, B. Q.; Zhao, C. X.; Liu, J. N.; Zhang, Q. Electrosynthesis of

hydrogen peroxide synergistically catalyzed by atomic Co–N_x–C sites and oxygen functional groups in noble-metal-free electrocatalysts. *Adv. Mater.* **2019**, *31*, 1808173.
[26] Tang, C.; Chen, L.; Li, H. J.; Li, L. Q.; Jiao, Y.; Zheng, Y.; Xu, H. L.; Davey, K.; Qiao, S. Z. Tailoring acidic oxygen reduction selectivity on single-atom catalysts via modification of first and second coordination spheres. *J. Am. Chem. Soc.* **2021**, *143*, 7819–7827.
[27] Gong, H. S.; Wei, Z. X.; Gong, Z. C.; Liu, J. J.; Ye, G. L.; Yan, M. M.; Dong, J. C.; Allen, C.; Liu, J. B.; Huang, K. et al. Low-coordinated Co-N-C on oxygenated graphene for efficient electrocatalytic H_2O_2 production. *Adv. Funct. Mater.* **2022**, *32*, 2106886.
[28] Shen, H. J.; Qiu, N. X.; Yang, L.; Guo, X. Y.; Zhang, K.; Thomas, T.; Du, S. Y.; Zheng, Q. F.; Attfield, J. P.; Zhu, Y. et al. Boosting oxygen reduction for high-efficiency H_2O_2 electrosynthesis on oxygen-coordinated Co-N-C catalysts. *Small* **2022**, *18*, 2200730.
[29] Li, C.; Zhao, D. H.; Long, H. L.; Li, M. Recent advances in carbonized non-noble metal-organic frameworks for electrochemical catalyst of oxygen reduction reaction. *Rare Met.* **2021**, *40*, 2657–2689.
[30] Da, Y. M.; Jiang, R.; Tian, Z. L.; Han, X. P.; Chen, W.; Hu, W. B. The applications of single-atom alloys in electrocatalysis: Progress and challenges. *SmartMat* **2023**, *4*, e1136.
[31] Zhu, Y. G.; Shang, C. Q.; Wang, Z. Y.; Zhang, J. Q.; Yang, M. Y.; Cheng, H.; Lu, Z. G. Co and N co-modified carbon nanotubes as efficient electrocatalyst for oxygen reduction reaction. *Rare Met.* **2021**, *40*, 90–95.
[32] Wang, X.; Yu, M. H.; Feng, X. L. Electronic structure regulation of noble metal-free materials toward alkaline oxygen electrocatalysis. *eScience* **2023**, *3*, 100141.
[33] Liu, H.; Li, J. J.; Arbiol, J.; Yang, B.; Tang, P. Y. Catalytic reactivity descriptors of metal-nitrogen-doped carbon catalysts for electrocatalysis. *EcoEnergy* **2023**, *1*, 154–185.
[34] Lin, L.; Su, P. Y.; Han, Y. T.; Xu, Y. M.; Ni, Q.; Zhang, X. Y.; Xiong, P. X.; Sun, Z. M.; Sun, G. B.; Chen, X. B. Advances in regulating the electron spin effect toward electrocatalysis applications. *eScience* **2025**, *5*, 100264.
[35] Lazaridis, T.; Stühmeier, B. M.; Gasteiger, H. A.; El-Sayed, H. A. Capabilities and limitations of rotating disk electrodes versus membrane electrode assemblies in the investigation of electrocatalysts. *Nat. Catal.* **2022**, *5*, 363–373.
[36] Ahn, C. Y.; Park, J. E.; Kim, S.; Kim, O. H.; Hwang, W.; Her, M.; Kang, S. Y.; Park, S.; Kwon, O. J.; Park, H. S. et al. Differences in the electrochemical performance of pt-based catalysts used for polymer electrolyte membrane fuel cells in liquid half- and full-cells. *Chem. Rev.* **2021**, *121*, 15075–15140.
[37] Kim, O. H.; Ahn, C. Y.; Kang, S. Y.; Kim, S.; Choi, H. J.; Cho, Y. H.; Sung, Y. E. From half-cells to membrane-electrode assemblies: A comparison of oxygen reduction reaction catalyst performance characteristics. *Fuel Cells* **2019**, *19*, 695–707.
[38] Pang, Y. Y.; Xie, H.; Sun, Y.; Titirici, M. M.; Chai, G. L. Electrochemical oxygen reduction for H_2O_2 production: Catalysts, pH effects and mechanisms. *J. Mater. Chem. A* **2020**, *8*, 24996–25016.
[39] Zhang, G. X.; Wei, Q. L.; Yang, X. H.; Tavares, A. C.; Sun, S. H. RRDE experiments on noble-metal and noble-metal-free catalysts: Impact of loading on the activity and selectivity of oxygen reduction reaction in alkaline solution. *Appl. Catal. B: Environ.* **2017**, *206*, 115–126.
[40] Yu, Z. X.; Liu, C.; Deng, Y. Y.; Li, M. H.; She, F. X.; Lai, L.; Chen, Y.; Wei, L. Interfacial engineering of heterogeneous molecular electrocatalysts using ionic liquids towards efficient hydrogen peroxide production. *Chin. J. Catal.* **2022**, *43*, 1238–1246.
[41] Liu, W.; Zhang, C.; Zhang, J. J.; Huang, X.; Song, M.; Li, J. W.; He, F.; Yang, H. P.; Zhang, J.; Wang, D. L. Tuning the atomic configuration of Co-N-C electrocatalyst enables highly-selective H_2O_2 production in acidic media. *Appl. Catal. B: Environ.* **2022**, *310*, 121312.
[42] Hu, H. S.; Zhang, C.; Liu, W.; Qi, H. Y.; Wang, H. Y.; Wang, X. Y.; Zhang, L. L.; Liu, L.; Bao, L. P.; Alomar, M. et al. Coaxial metal-nitrogen-carbon single-atom catalysts boost acid hydrogen peroxide production. *Adv. Funct. Mater.* **2025**, *35*, 2419220.
[43] Xu, H.; Lv, X. H.; Wang, H. Y.; Ye, J. Y.; Yuan, J. Y.; Wang, Y. C.; Zhou, Z. Y.; Sun, S. G. Impact of pore structure on two-electron oxygen reduction reaction in nitrogen-doped carbon materials: Rotating ring-disk electrode vs. flow cell. *ChemSusChem* **2022**, *15*, e202102587.
[44] Zhang, C.; Zhang, J.; Zhang, J. J.; Song, M.; Huang, X.; Liu, W.; Xiong, M.; Chen, Y. Q.; Xia, S. W.; Yang, H. P. et al. Tuning coal into graphene-like nanocarbon for electrochemical H_2O_2 production with nearly 100% faraday efficiency. *ACS Sustainable Chem. Eng.* **2021**, *9*, 9369–9375.
[45] Li, L. Q.; Tang, C.; Zheng, Y.; Xia, B. Q.; Zhou, X. L.; Xu, H. L.; Qiao, S. Z. Tailoring selectivity of electrochemical hydrogen peroxide generation by tunable pyrrolic-nitrogen-carbon. *Adv. Energy Mater.* **2020**, *10*, 2000789.
[46] Wang, Y. L.; Shi, R.; Shang, L.; Peng, L. S.; Chu, D. W.; Han, Z. J.; Waterhouse, G. I. N.; Zhang, R.; Zhang, T. R. Vertical graphene array for efficient electrocatalytic reduction of oxygen to hydrogen peroxide. *Nano Energy* **2022**, *96*, 107046.
[47] Zhang, C.; Liu, W.; Song, M.; Zhang, J. J.; He, F.; Wang, J.; Xiong, M.; Zhang, J.; Wang, D. L. Pyranoid-O-dominated graphene-like nanocarbon for two-electron oxygen reduction reaction. *Appl. Catal. B: Environ. Energy* **2022**, *307*, 121173.
[48] Kim, H. W.; Ross, M. B.; Kornienko, N.; Zhang, L.; Guo, J. H.; Yang, P. D.; McCloskey, B. D. Efficient hydrogen peroxide generation using reduced graphene oxide-based oxygen reduction electrocatalysts. *Nat. Catal.* **2018**, *1*, 282–290.
[49] Han, G. F.; Li, F.; Zou, W.; Karamad, M.; Jeon, J. P.; Kim, S. W.; Kim, S. J.; Bu, Y. F.; Fu, Z. P.; Lu, Y. L. et al. Building and identifying highly active oxygenated groups in carbon materials for oxygen reduction to H_2O_2. *Nat. Commun.* **2020**, *11*, 2209.
[50] Huang, Y. Z.; Zhang, C.; Wang, X. Y.; Wu, Y. J.; Lv, J.; Zhang, J.; Shen, W. Q.; Lu, X. Synergistic single-atom and clustered cobalt sites on N/S co-doped defect nano-carbon for efficient H_2O_2 electrosynthesis. *Nano-Micro Lett.* **2025**, *17*, 142.
[51] Gewirth, A. A.; Varnell, J. A.; DiAscro, A. M. Nonprecious metal catalysts for oxygen reduction in heterogeneous aqueous systems. *Chem. Rev.* **2018**, *118*, 2313–2339.
[52] Yasin, G.; Ibrahim, S.; Ajmal, S.; Ibraheem, S.; Ali, S.; Nadda, A. K.; Zhang, G. X.; Kaur, J.; Maiyalagan, T.; Gupta, R. K. et al. Tailoring of electrocatalyst interactions at interfacial level to benchmark the oxygen reduction reaction. *Coord. Chem. Rev.* **2022**, *469*, 214669.
[53] Liu, J. Y.; Wan, X.; Liu, S. Y.; Liu, X. F.; Zheng, L. R.; Yu, R. H.; Shui, J. L. Hydrogen passivation of M-N-C (M = Fe, Co) catalysts for storage stability and ORR activity improvements. *Adv. Mater.* **2021**, *33*, 2103600.
[54] Xia, G. S.; Tian, Y. D.; Yin, X. M.; Yuan, W. H.; Wu, X. C.; Yang, Z. X.; Yu, G.; Wang, Y. J.; Wu, M. B. Maximizing electrochemical hydrogen peroxide production from oxygen reduction with superaerophilic electrodes. *Appl. Catal. B: Environ.* **2021**, *299*, 120655.
[55] Zhang, Q. Z.; Zhou, M. H.; Ren, G. B.; Li, Y. W.; Li, Y. C.; Du, X. D. Highly efficient electrosynthesis of hydrogen peroxide on a superhydrophobic three-phase interface by natural air diffusion. *Nat. Commun.* **2020**, *11*, 1731.